J Mater Sci: Mater Electron (2026) 37:537

Tailoring the microstructure and electrical performance of ZnO varistor ceramics via $SrTiO_3$ doping

Norni Hidayawati Mat Daud[1,2], Muhamad Syaizwadi Shaifudin[1], Idza Riati Ibrahim[2], Nursabrina Amirah Mohd Nasir[1], Abdul Mu'iz Aniq Aiman Mohd Suhaimi[1], Mohd Sabri Mohd Ghazali[1,*], Nor Hazmin Sabri[1], and Mohd Hafiz Mohd Zaid[3]

[1] *Faculty of Science and Marine Environment, Universiti Malaysia Terengganu, Kuala Nerus, 21030 Kuala Terengganu, Terengganu, Malaysia*

[2] *Centre for Pre-University Studies, Universiti Malaysia Sarawak, 94300 Kota Samarahan, Sarawak, Malaysia*

[3] *Faculty of Science, Universiti Putra Malaysia, UPM, 43400 Serdang, Selangor, Malaysia*

Received: 19 January 2026
Accepted: 3 March 2026

ABSTRACT

In this study, the effect of strontium titanate ($SrTiO_3$) doping on the microstructural evolution and electrical characteristics of zinc oxide (ZnO) varistors is investigated. The ZnO-$SrTiO_3$ ceramic was synthesized using a two-stage sintering technique. Microstructural analysis using X-Ray Diffraction (XRD) reveals the formation of Zn_2TiO_4 spinel phase, while scanning electron microscopy (SEM) and energy dispersive X-ray (EDX) analysis confirm the segregation of Sr-rich secondary phases at the grain boundaries and triple points. The microstructure and densification were significantly enhanced at the optimum $SrTiO_3$ concentration, thereby improving the electrical properties of the fabricated varistor, with the nonlinear coefficient (α) increasing to 5.49 and the leakage current density (J_L) decreasing to 298 μA/cm^2. This investigation provides a deeper understanding of dopants' influence on ZnO varistors, thereby facilitating the development of more effective and reliable surge protective devices, especially for low-voltage applications.

1 Introduction

The increasing demand for electrical and electronic systems, ranging from low-voltage appliances to high-voltage industrial equipment, emphasizes the critical need for adequate protection against electrical surges. These surges, which may be caused by lightning, high-energy switching, or electrostatic discharge, deliver an oversupply of voltage within microseconds to milliseconds and can seriously damage electrical equipment. Therefore, advanced surge protection devices, such as metal oxide varistors, are necessary, as they play an important role in diverting excess current to ground and absorbing surge energy to provide safe protection.

Historically, silicon carbide (SiC) was among the earliest materials used for varistors before zinc oxide

Address correspondence to E-mail: mohdsabri@umt.edu.my

https://doi.org/10.1007/s10854-026-16945-2
Published online: 11 March 2026

(ZnO) varistors were developed in the 1970s [1]. Since then, many commercial applications have adopted ZnO varistors due to their exceptional ability to suppress voltage surges. To date, numerous studies have investigated their properties in depth. In brief, a varistor's performance mainly depends on its composition and microstructure. Thus, both material formulation and processing conditions must be carefully controlled to achieve high-energy absorption and strong nonlinearity.

Among the numerous dopants used in ZnO varistors, bismuth oxide (Bi_2O_3) has long been recognized as a significant varistor former. The reason is that it can facilitate the formation of active grain boundaries during sintering and act as a liquid-phase sintering aid, lowering the sintering temperature and enhancing densification [2]. It also contributes to the formation of double Schottky barriers at grain boundaries, which are crucial for non-ohmic behavior [3]. However, Bi_2O_3 has several drawbacks. Notably, it tends to evaporate during high-temperature sintering, which may cause poor compositional control and inconsistent performance [4]. To enhance the properties of ZnO-Bi_2O_3-based varistors, additives such as Sb_2O_3, Co_3O_4, and MnO_4 are frequently incorporated to control grain growth and enhance barrier formation [5–8]

Previous studies have shown that incorporating strontium-based additives such as SrO or $SrCO_3$ into Bi_2O_3-doped ZnO systems can significantly influence microstructural development and electrical performance. The addition of $SrCO_3$, especially at higher concentrations, leads to the formation of $Bi_6Sr_2O_{11}$ secondary phases that segregate to grain boundaries, thereby improving electrical properties [9]. However, unlike the common approaches, Rohini et al. used Sr as an additive. Specifically, instead of using $SrCO_3$ with Bi_2O_3 as an additive, Rohini et al. included SrO as a major additive, resulting in an increase in the grain-boundary active area, which significantly improves nonlinearity [10].

Another additive that has attracted attention is TiO_2. In most studies, this material has been utilized as a promoting additive to produce low-voltage ZnO-Bi_2O_3 ceramics. By accelerating solid-phase mass transfer, the grain size can be greatly improved, and the threshold voltage can be reduced [11]. Similarly, TiO_2 acts as a grain growth promoter in ZnO-V_2O_5-based varistors [12] however, in ZnO-Pr_6O_{11}-based varistors, TiO_2 inhibits grain growth, highlighting its different role depending on the base system [13].

Due to the limitations of current varistor formers, such as the volatility of Bi_2O_3 during high-temperature sintering, the scarcity of Pr_6O_{11}, which makes it more expensive, and the environmental toxicity associated with V_2O_5, there has been interest in exploring alternative materials with stable, cost-effective, and environmentally friendly properties. Perovskite-structured compounds have attracted considerable attention as potential varistor formers or performance enhancers in ZnO-based varistors. Materials such as $BaTiO_3$, $CaMnO_3$, $PrMnO_3$, and $CaSiO_3$ have been investigated for their ability to improve the nonlinear electrical characteristics and thermal stability of varistors [14–17].

Among these, strontium titanate ($SrTiO_3$), a well-known perovskite with a high-dielectric constant and thermal stability, has primarily been used as an additive in SnO_2-based and $CaCu_3Ti_4O_{12}$-based varistors to improve their electrical characteristics [18, 19]. However, the influence of $SrTiO_3$ on ZnO-based varistors remains largely unexplored. Furthermore, selecting the perovskite oxide $SrTiO_3$ as a dopant, rather than individual oxides such as SrO, aims to achieve precise microstructural control and enhanced electrical stability for a low-voltage varistor, as $SrTiO_3$ is chemically more stable than SrO, which is hygroscopic and readily reacts with air. The chemically stable lattice of $SrTiO_3$ prevents the formation of secondary hydroxides during powder processing and milling. Therefore, the current work examines how varying $SrTiO_3$ concentrations affect the microstructure and electrical performance of ZnO-based varistor ceramics.

2 Experimental procedure

In the present study, analytical-grade ZnO (≥ 99% purity) and $SrTiO_3$ (≥ 99.5% purity) nanopowders were used as raw materials for the preparation of varistor samples. The raw powder suppliers were Sigma Aldrich and XFNano. These raw powders were weighed based on the molar composition of (100-x) mol % ZnO + x mol % $SrTiO_3$, where x = 0, 0.5, 1.0, 1.5, 2.0, and then milled using a planetary ball mill (POWTEQ BM6 Pro) for 3 h. 2 wt % of polyvinyl alcohol were added to the milled powder as a binder and then dried at 90 °C for 2 h. The dried powder was ground in an agate mortar, sieved through a 50 μm sieve, and pressed into a pellet at 2.6 T/min for 5 min using a hydraulic press machine. The pellets, with a 10 mm

diameter and 1 mm thickness, were sintered using a two-stage sintering technique in a high-temperature furnace. The sintering process was initially carried out in an air-conditioned environment by increasing the temperature to 1300 °C at a rate of 10 °C min^{-1} and soaking at 1300 °C for 5 min, followed by cooling to a temperature of 900 °C at a rate of 3 °C min^{-1} and constant heating at 900 °C for 2 h. The main advantage of this two-stage sintering technique is that it favours the grain boundary diffusion. Still, it constrains grain boundary migration, ensuing in full densification and controlled grain growth in the sintered pellets [20]. Silver paste was coated onto the upper and bottom surfaces of the varistor samples after sintering. Afterward, the samples were heated to 600 °C for ten minutes to create electrodes.

The crystallographic phases of the sintered pellets were characterized using X-ray diffraction (XRD, Rigaku MiniFlex II) equipped with CuKα radiation source, with 2θ ranging from 20° to 80°. The data were analyzed using SmartLab Studio II software. Peak positions were obtained using a second-derivative peak search (σ cut = 3.0) followed by split pseudo-Voigt profile fitting with automatic background refinement. The lattice parameters, a and c of hexagonal wurtzite ZnO were determined from peak-position analysis using Bragg's law and the hexagonal interplanar spacing relations rather than full-pattern refinement. The plane spacing equation for the hexagonal structure [21]:

$$\frac{1}{d^2} = \frac{4}{3}\left(\frac{h^2 + hk + k^2}{a^2}\right) + \frac{l^2}{c^2} \tag{1}$$

where Bragg's law ($\lambda = 2d_{hkl} \sin \theta_{hkl}$) can be used to find the interplanar spacing, d.

The lattice parameter, a, was calculated from the (100) reflection, while c was calculated from the (002) reflection. The derived lattice constants a_{100} and c_{002} were validated by the (101) reflection, where the calculated d_{101} will be compared to the measured d_{101} through its deviation to determine the reliability of the data.

The unit cell volume, V, of the hexagonal structure was determined from the lattice parameters a and c using the formula [22]:

$$V = \frac{\sqrt{3}}{2}a^2c \tag{2}$$

Scanning electron microscopy (SEM) combined with energy dispersive X-ray (EDX) spectroscopy was employed to examine the morphology of the sintered pellets. A thin layer of Au was applied to the samples' surfaces to minimize charging effects and enhance image quality. An image analysis application (ImageJ) was used to calculate the average grain size from the SEM micrographs. The average grain size was calculated by considering more than 150 grains. Additionally, an electronic densimeter (MDS-300) was used to measure the densities of sintered pellets.

A Source-Measure Unit (SMU) (Keithley 2410) was employed to measure electrical properties, including current density–electric field (J-E) characteristics. Using the J-E graph data, the nonlinear coefficient, α, was computed as follows [23]:

$$\alpha = \frac{\log J_2 - \log J_1}{\log E_2 - \log E_1} \tag{3}$$

where E_1 and E_2 are the applied electric fields for certain current densities $J_1 = 0.1$ mA/cm^2 and $J_2 = 1.0$ mA/cm^2, respectively. The electric field at which $J = 1.0$ mA/cm^2 is known as the breakdown electric field, E_b, while leakage current density, J_L, is measured at an electric field equivalent to 80% of the breakdown electric field ($0.80E_b$). The barrier height (φ_B) was determined using the formula below [24]:

$$J = AT^2 \exp\left[\frac{\beta E^{\frac{1}{2}} - \varphi_B}{k_B T}\right] \tag{4}$$

where the value of Richardson's constant for ZnO, A = 30 A/cm^2K^2, Boltzmann constant $k_B = 8.617 \times 10^{-5}$ eV/K, and absolute temperature, $T = 300$ K. Meanwhile, the gradient from the graph of ln J vs $E^{0.5}$ is used to calculate β, a constant associated with the potential barrier width.

3 Results and discussion

The XRD pattern of the samples with different $SrTiO_3$ concentrations is shown in Fig. 1a. It shows that both ZnO and $SrTiO_3$-doped ZnO ceramics samples are dominated by a sharp and strong diffraction peak, which corresponds to the hexagonal wurtzite structure of the ZnO phase (JCPDS no. 01–080-3004). The presence of $SrTiO_3$ phase (JCPDS no. 01–079-0174) and spinel Zn_2TiO_4 secondary phase (JCPDS no.

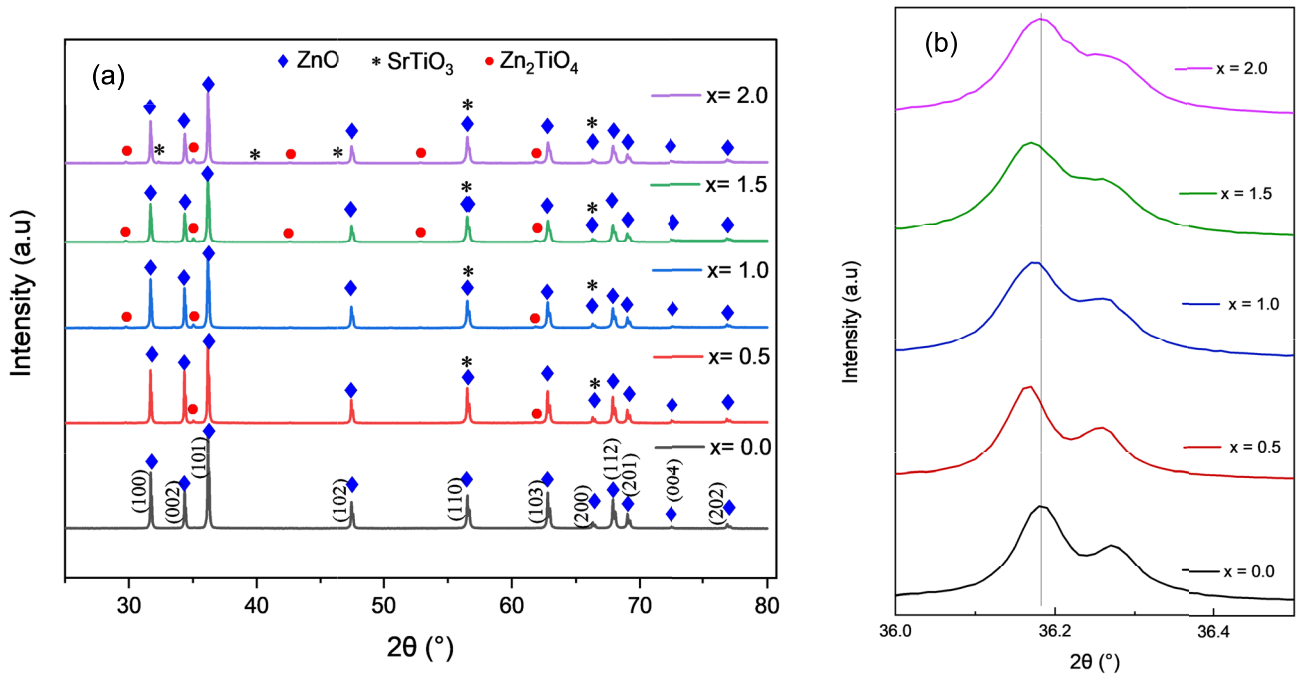

Fig. 1 **a** XRD patterns of ZnO doped with different mol% concentrations of $SrTiO_3$: $x = 0.0$, 0.5, 1.0, 1.5, and 2.0. **b** Detailed observation of the ZnO (101) peak

01–086-0155) was observed after the addition of $SrTiO_3$ dopant. The Zn_2TiO_4 phase became more pronounced as the concentration of $SrTiO_3$ was increased, implying that the addition of $SrTiO_3$ promotes the formation of secondary phases, likely due to Ti ion diffusion into the ZnO lattice during sintering [13]. However, there are no peaks corresponding to Sr-rich compounds other than that of $SrTiO_3$, suggesting the remaining Sr ions are dispersed around ZnO, or exist in a Sr-rich amorphous phase, or are too small in volume, making them fall below the detection limit of XRD [25]. Meanwhile, a more distinct $SrTiO_3$ phase was observed as the sample reached a $SrTiO_3$ dopant concentration of 2.0 mol %. Moreover, the characteristic peak intensity of ZnO was found to decrease gradually with increasing $SrTiO_3$ concentration, similar to the findings of Zhao et al. [26].

Another significant observation in the XRD patterns was a shift in the peak position of the (101) plane to $2\theta = 36.18°$, as shown in Fig. 1b. This shift suggests changes in the lattice parameters of the ZnO phase, as tabulated in Table 1. The peaks initially shifted slightly to the left (lower 2θ angles), indicating an expansion of the ZnO lattice. This expansion could be attributed to the substitution of larger Sr^{2+} ions into the ZnO lattice, or due to the segregation of $SrTiO_3$ [27]. The incorporation of these ions into the ZnO lattice affected the lattice strain and distortion,

Table 1 Lattice parameters, ratio of lattice parameters, unit cell volume, and interplanar spacing of ZnO with different mol% $SrTiO_3$ dopant concentration

$SrTiO_3$ concentration (mol%)	*a* (Å)	*c* (Å)	*c*/*a* ratio	Unit cell volume (Å^3)	Interplanar spacing d_{101} calculated (Å)	Interplanar spacing d_{101} measured (Å)	Δd/d (%)
0	3.2568	5.2167	1.6018	47.92	2.4810	2.4805	0.0202
0.5	3.2584	5.2188	1.6016	47.988	2.4822	2.4816	0.0242
1	3.2579	5.2182	1.6017	47.966	2.4818	2.4812	0.0242
1.5	3.2588	5.2172	1.6009	47.983	2.4822	2.4815	0.0282
2	3.258	5.216	1.6009	47.949	2.4816	2.4808	0.0322

resulting in peak shifting. However, at $x = 2.0$ mol%, the peaks shifted back to the right (higher 2θ angles), suggesting a lattice contraction. This reversal peak shift may be due to the elevated $SrTiO_3$ doping concentration, which results in the segregation of Sr^{2+} and Ti^{4+} ions at the grain boundaries [28]. These segregations contribute to the detection of more $SrTiO_3$ peaks.

Therefore, the doping of $SrTiO_3$ into the ZnO system initiates a solid-state reaction during sintering and can be presented by the following chemical mechanism:

$$2ZnO + SrTiO_3 \rightarrow Zn_2TiO_4 + SrO \quad (5)$$

As the Ti^{4+} ions from the $SrTiO_3$ precursor react with the ZnO matrix to form the thermodynamically stable spinel phase Zn_2TiO_4, the Sr^{2+} ions are liberated. Due to the large size difference, the ZnO lattice can only accommodate a very small fraction of Sr^{2+}. Once the solubility limit is reached, the excess Sr^{2+} ions are expelled from the grain interior during grain growth. These ions migrate toward high-energy regions, such as grain boundaries and triple points, to minimize the system's total elastic strain energy. This explains the Sr-rich phases observed at the junction of ZnO grains in the next SEM–EDX analysis.

Figure 2 shows the SEM micrograph and grain-size distribution histograms to illustrate the microstructural evolution of ZnO-$SrTiO_3$ ceramics with varying doping concentrations. The histogram shows a log-normal distribution of grain size, while the micrograph shows three main structures: (1) the ZnO grains, (2) the spinel phase, and (3) the Sr-rich phase. It was found that the distributions of spinel and Sr-rich phases vary with increasing $SrTiO_3$ concentration. At a lower concentration of $SrTiO_3$, there are only two apparent phases observed, which are designated as the ZnO phase and the spinel phase. The ZnO grains exhibited a large polyhedral shape while the spinel phase formed a small diamond-like structure, as labelled in Fig. 2b. As the dopant concentration increases, more spinel phases were detected crystallizing at both ZnO grains and grain boundaries. In contrast, the $SrTiO_3$ phase was detected only near the Sr-rich phases at the grain boundaries and triple points, as shown in Fig. 2c. The formation of these spinel secondary phases and Sr-rich phases with increasing $SrTiO_3$ dopant has restricted grain boundary migration via Zener pinning, thereby inhibiting grain growth. Therefore, a clear decreasing trend in average grain size was observed with increasing $SrTiO_3$ content. The same reduction in grain size was observed when SrO was used as an additive in ZnO-based varistors [10]. The same trend was also observed, where ZnO grain growth decreased gradually due to the formation of the Zn_2TiO_4 spinel phase [7]. In this work, controlled grain growth results in a uniform, monodisperse distribution of ZnO grains, which is observed at lower $SrTiO_3$ doping concentrations.

Further increasing the dopant concentration reveals additional Sr-rich phases that form a large cluster, as also observed in Fig. 2e. The formation of non-uniform, larger clusters along the ZnO grains disrupts the previously uniform grain structure. This anomaly may be due to the excessive accumulation of Sr ions that are difficult to enter the ZnO lattice due to its larger ionic radius, the Sr ions are enriched at the grain boundaries [29], forming larger particles or clusters. These clusters of significant segregation of Sr-rich compounds might locally alter the grain boundary energy, creating uneven driving forces for grain growth and facilitating abnormal grain growth in certain regions [30].

The elemental composition and distribution of Zn, Sr, Ti, and O in a sample with uniform and non-uniform grain structure are illustrated in Fig. 3 through EDS analysis. Their atomic percentages are tabulated in Table 2. A uniform microstructure of ZnO doped with 1.5 mol % of $SrTiO_3$ shows that the Sr element was mainly detected segregating at the triple point and grain boundary areas, as illustrated in Fig. 3a. The segregation is possibly due to the greater ionic radius of Sr ions (1.18 Å) compared to Zn ions (0.74 Å), which limits its solid solubility in the ZnO lattice. A similar observation was also reported by Yongyavanich et al. [31]. The presence of Sr and Ti at the grain boundary indicates that the interaction between ZnO and $SrTiO_3$ during sintering has led to the formation of the secondary phase Zn_2TiO_4, which inhibits ZnO grain growth and further reduces its grain size. The EDS analysis aligns well with the XRD findings, confirming the presence of Zn_2TiO_4 and $SrTiO_3$ peaks, indicating that $SrTiO_3$ was doped into ZnO. With increased $SrTiO_3$ doping, the mapping of more Sr was observed, indicating the segregation of Sr-rich phases around ZnO grains, as shown in Fig. 3b. This finding corresponds to the disruption of grain boundary uniformity observed in the SEM micrographs, further affirming the earlier analysis.

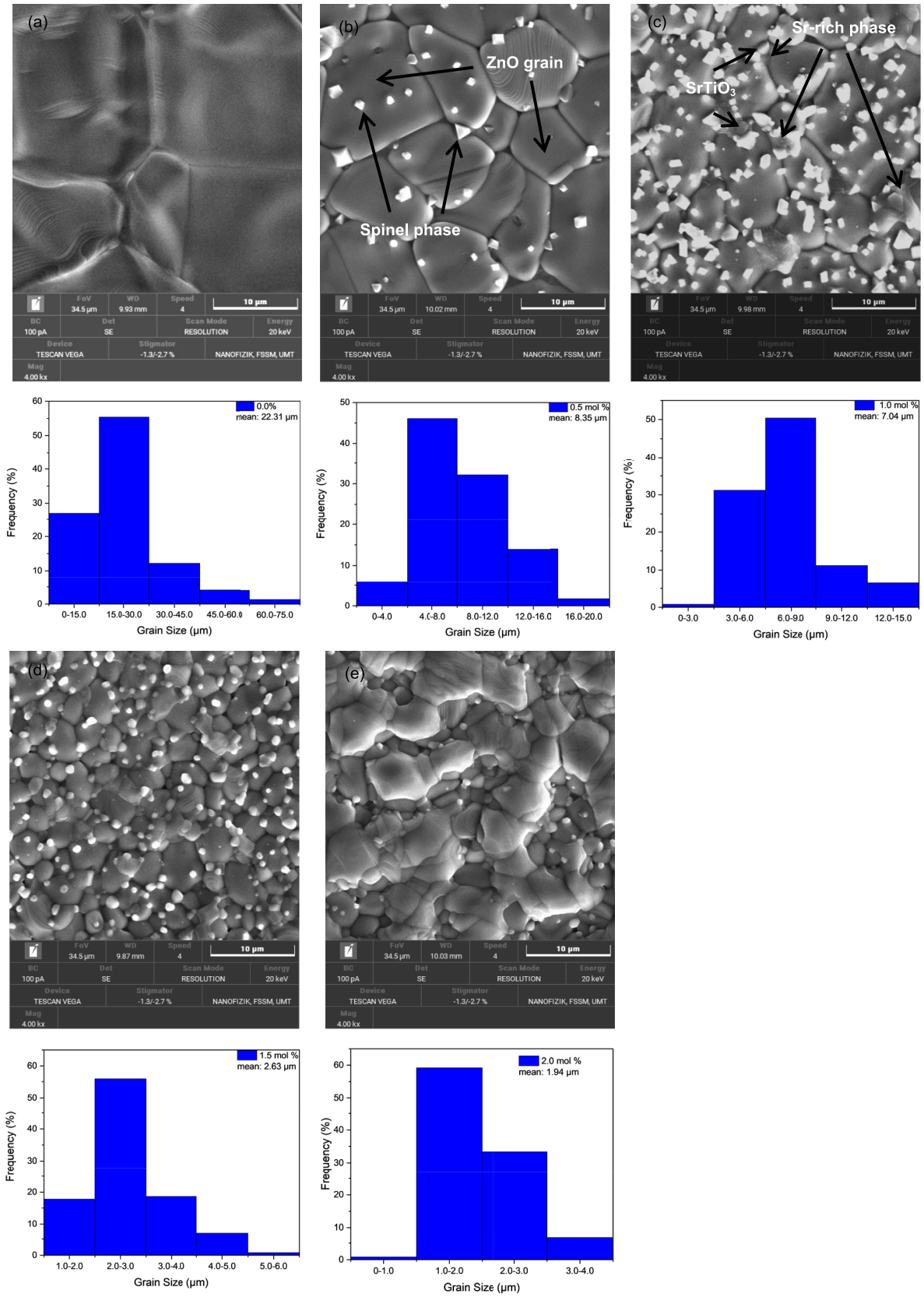

Fig. 2 SEM images of ZnO doped with different mol concentration of $SrTiO_3$, **a** 0.0, **b** 0.5, **c** 1.0, **d** 1.5 and **e** 2.0

The addition of $SrTiO_3$ dopant into ZnO ceramics not only changes the microstructure but also improves the densification of the samples. Table 3 shows that the measured density for pure ZnO is 5.31 g/cm^3, which is less than the theoretical density of ZnO, 5.61 g/cm^3, their relative density is only 94.65%. However, the measured density increased gradually as the $SrTiO_3$ dopant concentration rose to 1.5 mol %, which does not follow the theoretical density trend. Nevertheless, the relative density increases from 97.85% to 99.82%, then slightly decreases to 97.84% as $SrTiO_3$ increases further, as illustrated in Fig. 4. The improved densification was greatly influenced by the addition of $SrTiO_3$ as a dopant to ZnO ceramics via two-stage sintering.

During the first stage of the two-stage sintering method, a high-sintering temperature of 1300 °C increases atomic diffusion rates. As atoms diffuse and migrate, they facilitate particle bonding by creating necks between adjacent particles [35]. The pores start to shrink, and the grain boundaries become mobile, leading to the growth of ZnO grains. However, as the holding time was only 5 min, limited grain growth and densification occurred in this stage. This condition also applies to $SrTiO_3$, which has a limited time to grow. Thus, some of the $SrTiO_3$ interact with ZnO and form secondary Zn_2TiO_4, while the others remain as $SrTiO_3$ and form a Sr-rich phase. This dopant and secondary phase filled the pores in the grain-boundary region.

In the second stage of sintering, the grain growth rate was controlled to prevent excessive coarsening, as a lower sintering temperature of 900 °C was used [36]. The restriction of grain growth due to the presence of $SrTiO_3$ at grain boundaries, which acts as a pinning agent, contributed to a well-maintained fine-grained microstructure with better particle packing. The continuous densification for two hours, combined with the controlled grain growth, successfully produced a higher overall density despite the smaller grain sizes.

As a result, at 1.5 mol % $SrTiO_3$, the relative density reached its maximum value of 99.82%, showing minimal porosity and a highly dense material. However, beyond 2.0 mol % $SrTiO_3$, the relative density significantly dropped to 97.84%, despite the continued refinement of ZnO grains. This decline is due to the excessive addition of $SrTiO_3$, which leads to the agglomeration of Sr-rich compounds that disrupt the continuity of the ZnO matrix. These agglomerations introduce additional porosity and act as barriers to mass transport during sintering, hindering densification. Therefore, the material retains higher porosity, resulting in a lower relative density.

The *J-E* characteristics of the ZnO varistor samples with varying $SrTiO_3$ concentrations are shown in Fig. 5. The breakdown electric field E_b, nonlinearity coefficient α, potential barrier φ_B, and leakage current density J_L, which were determined from the J-E curve, are listed in Table 4. The nonlinear coefficient, α, reflects the material's ability to handle voltage surges, which is enhanced by the potential barriers at the grain boundaries. It was found that the nonlinear coefficient α, potential barrier φ_B, and breakdown electric field E_b increased with increasing $SrTiO_3$ content from 0 to 1.5 mol% and decreased with further increases in $SrTiO_3$ concentration to 2 mol%.

The inclusion of $SrTiO_3$ at 0.5–1.5 mol% significantly increased the density of the ZnO ceramic, resulting in a finer, more homogeneous grain microstructure. The improved densification, characterized by reduced porosity and better grain packing, enhances the varistor's mechanical strength and thermal conductivity, crucial for dissipating heat during surge events and preventing thermal runaway [37]. The grain refinement caused by the Sr-rich phase at triple points physically prevents ZnO grains from merging. It led to a smaller average grain size d, directly contributing to an increased breakdown electric field E_b, from 0.37 to 2.16 V/mm. Fundamentally, the breakdown electric field can be approximated by the following relationship:

$$E_b = \frac{V_{gb}}{d} \tag{6}$$

where V_{gb} is the average breakdown voltage across a single grain boundary, and d is the average grain size [9]. A smaller average grain size d translates directly to a greater number of grain boundaries in series for a given varistor thickness. As these numerous boundaries act as individual resistive barriers, their increased count effectively hinders electron flow, causing an accumulation of a higher overall breakdown voltage per unit length, which manifests as an increased E_b.

Moreover, the addition of $SrTiO_3$ has a dual effect on the microstructure and electrical properties of ZnO. Specifically, a portion of the $SrTiO_3$ incorporated into the ZnO grains may form a solid solution, while another portion may segregate at the ZnO grain boundaries. Kai Wang and Jianke Liu stated that dopant segregation at ZnO grain boundaries

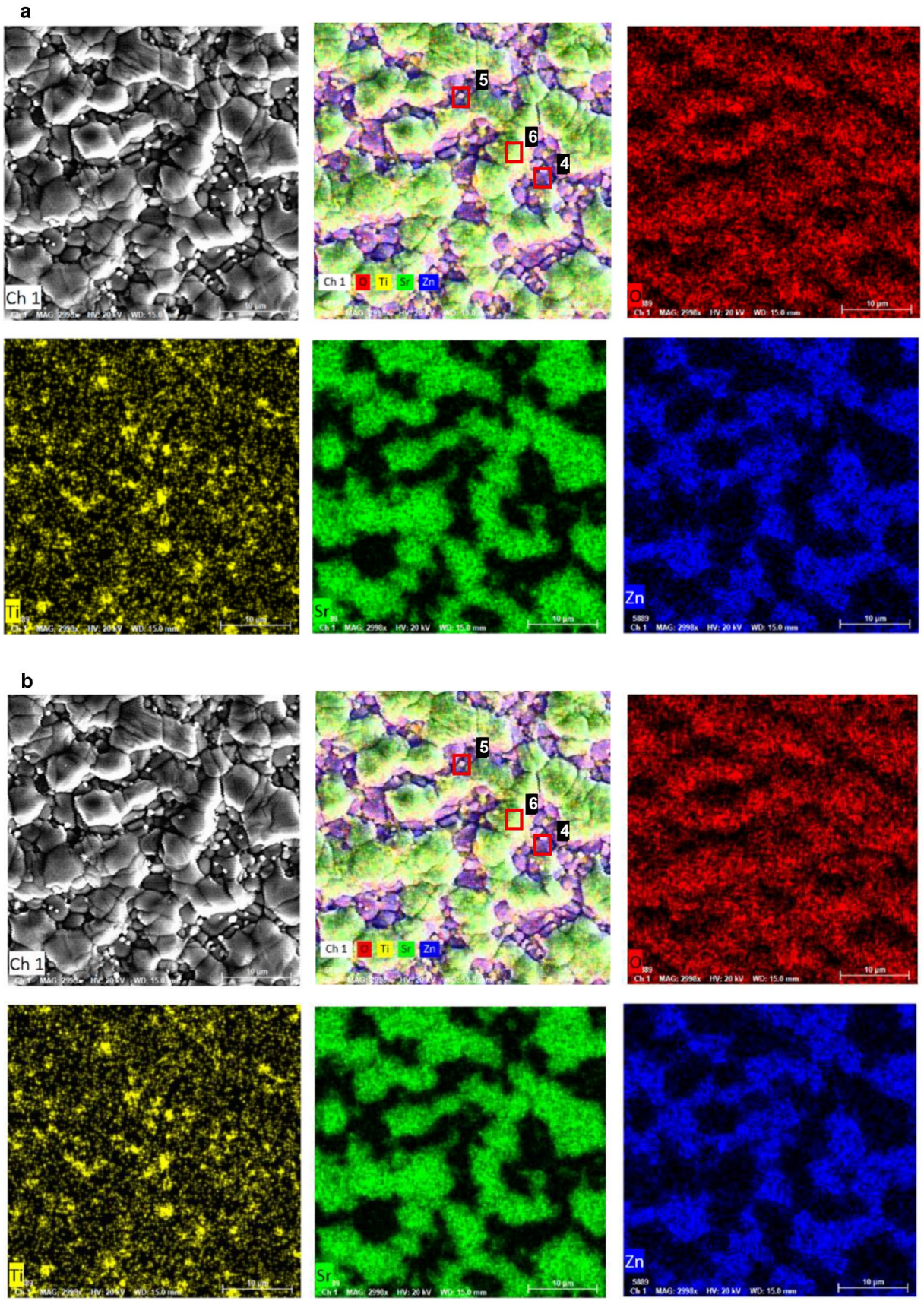
a
Ch 1
5
6
4
Ch 1 O Ti Sr Zn
O
Ti
Sr
Zn
b
Ch 1
5
6
4
Ch 1 O Ti Sr Zn
O
Ti
Sr
Zn

◂**Fig. 3** **a** EDS mapping of ZnO with 1.5 mol% $SrTiO_3$ concentration. **b.** EDS mapping of ZnO with 2.0 mol% $SrTiO_3$ concentration

effectively enhances the formation of acceptor-like states [38, 39]. The formation of acceptor-like states at grain boundaries traps free electrons, leading to a depletion layer. This layer forms on both sides of the grain boundary, is depleted of free charge carriers, and promotes the formation of double Schottky barriers in these regions [40].

Consequently, the observed increase in the potential barrier, from 0.61 to 0.69 eV, is attributed not only to the increased number of grain boundaries that electrons must traverse but also to the enhanced formation of these double Schottky barriers as the $SrTiO_3$ content increases. In this work, the Ti^{4+} dissolving into the ZnO grain boundary causes the defect reaction of:

$$TiO_2 \xrightarrow{ZnO} Ti_{Zn}^{\bullet\bullet} + 2O_O^x + V_{Zn}'' \quad (7)$$

This reaction is crucial for electrical performance as it generates Zinc vacancies V_{Zn}'' which serves as the primary acceptor defect. According to Double Schottky Barrier (DSB) model, these V_{Zn}'' migrate towards the intergranular layer, thus enhancing the grain boundary barrier. Therefore, the potential barrier is elevated, coupled with a fine, dense, and homogeneous grain microstructure, significantly enhancing the nonlinear coefficient.

The nonlinearity in the ZnO doped with $SrTiO_3$ content was clearly evident in the *J-E* curve in Fig. 5. The curve showed two main conduction regions: the pre-breakdown region and the breakdown region. The pre-breakdown region is where voltages are below the threshold voltage, in which the material exhibits high resistance and minimal current flow. In comparison, the breakdown region is where the resistance drops drastically, causing the current to increase suddenly. The "knee" of the curve can be observed in this breakdown region, in which the sharpness of this knee directly correlates with the nonlinearity coefficient, α [41] and is often determined by the following empirical relationship:

$$I = KV^{\alpha} \quad (8)$$

where I is current, V is voltage, and K is a constant. The sharper "knee" observed in Fig. 5 indicates the increase in the nonlinear coefficient α from 1.72 to 5.49 as the $SrTiO_3$ content increases. A higher α is required for a pronounced nonlinear response for effective voltage clamping. While the optimal nonlinear coefficient achieved in this study ($\alpha = 5.49$) is lower than that reported for $SrCO_3$-doped quaternary systems ($\alpha = 29.37$) [9], this difference arises from the fundamentally different electrical regimes targeted by the two systems. High-voltage varistors utilizing $SrCO_3$ and Bi_2O_3 rely on the formation of complex secondary phases, such as $Bi_6Sr_2O_{11}$, which create extremely high, thick potential barriers, resulting in breakdown voltages exceeding 1000 V. In contrast, the ZnO-$SrTiO_3$ system in this study is uniquely optimized for low-voltage microelectronic protection, achieving an E_{1mA} of only 2.16 V/mm.

In the low-voltage regime, the potential barrier at the grain boundary must be responsive and thermally stable to enable low-voltage triggering. The use of $SrTiO_3$ as a pre-reacted perovskite precursor facilitates the formation of Zn_2TiO_4 intergranular pinning agents and Sr-rich heterojunctions that provide a gradual but highly stable nonlinear transition. While the $SrCO_3$ system offers superior nonlinearity for high-power grids, it would be electrically 'blind' to the low-voltage transients found in modern integrated circuits. Thus, the α value of 5.49 indicates a significant and functional nonlinear response in a low-voltage ceramic, providing a unique advantage for protecting sensitive low-power components where traditional high-α compositions are ineffective.

Meanwhile, J_L also shows promising results with the addition of a $SrTiO_3$ dopant. As α, E_b and φ_B increased, J_L consistently decreased with increasing $SrTiO_3$ dopant concentration from 0.0 to 1.5 mol%. This inverse relationship is a critical indicator of enhanced varistor quality, as the increasingly elevated potential barrier developed at the grain boundaries due to $SrTiO_3$ incorporation presents a greater energetic impediment to electron flow in the pre-breakdown region. This effectively minimizes unintended current bypass through the material, ensuring that the varistor maintains its highly resistive "off" state more efficiently.

However, the experimental results revealed a crucial turning point. When the $SrTiO_3$ concentration reached 2.0 mol %, the microstructure degraded significantly, becoming inhomogeneous, with Sr-rich phases appearing throughout the grains. These excessive Sr-rich phases disrupt the finely tuned varistor mechanism. This might cause the barrier to become

Table 2 Atomic percentage of Fig. 3(a) and 3(b)

Sample with x $SrTiO_3$	Site	Atomic percentage (%)			
		Zn	Sr	Ti	O
$x=1.5$	1	53.02	0.02	0.08	46.88
	2	29.79	0.93	7.50	61.79
	3	17.04	14.75	1.32	66.90
$x=2.0$	4	64.89	0.48	0.43	34.21
	5	42.89	1.50	7.04	48.58
	6	6.53	20.62	0.50	72.35

inherently less resistive, thinner, or contain defects that lower its effective height, directly leading to a slight decrease in the potential barrier height.

The presence of an inhomogeneous microstructure means that the grain boundaries are no longer uniformly distributed or possess consistent electrical characteristics [42]. This leads to the formation of defective pathways within the ceramic body, where breakdown can occur prematurely at lower electric fields [43]. Current tends to localize and flow preferentially through these weaker pathways, bypassing most of the active, high-resistance grain boundaries [44]. Consequently, this non-uniform breakdown broadens the "knee" in the I-V curve, leading to a decreased nonlinear coefficient, α. The results highlight that while $SrTiO_3$ is beneficial as a dopant, its concentration must be precisely controlled to achieve optimal varistor performance while avoiding detrimental secondary phase formation and microstructural inhomogeneity. The electrical performance of ZnO-$SrTiO_3$ system was compared with recent studies targeting low-voltage applications, such as transition-metal-doped

Table 3 Average grain size and densities of ZnO varistor with various $SrTiO_3$ concentrations

$SrTiO_3$ concentration (mol%)	Average grain size (μm)	Measured density (g/cm^3)	Theoretical density (g/cm^3) [32]	Relative density (%) [33]
0	22.31	5.31	5.61 [34]	94.65
0.5	8.35	5.48	5.60	97.85
1.0	7.04	5.52	5.59	98.74
1.5	2.63	5.57	5.58	99.82
2.0	1.94	5.45	5.57	97.84

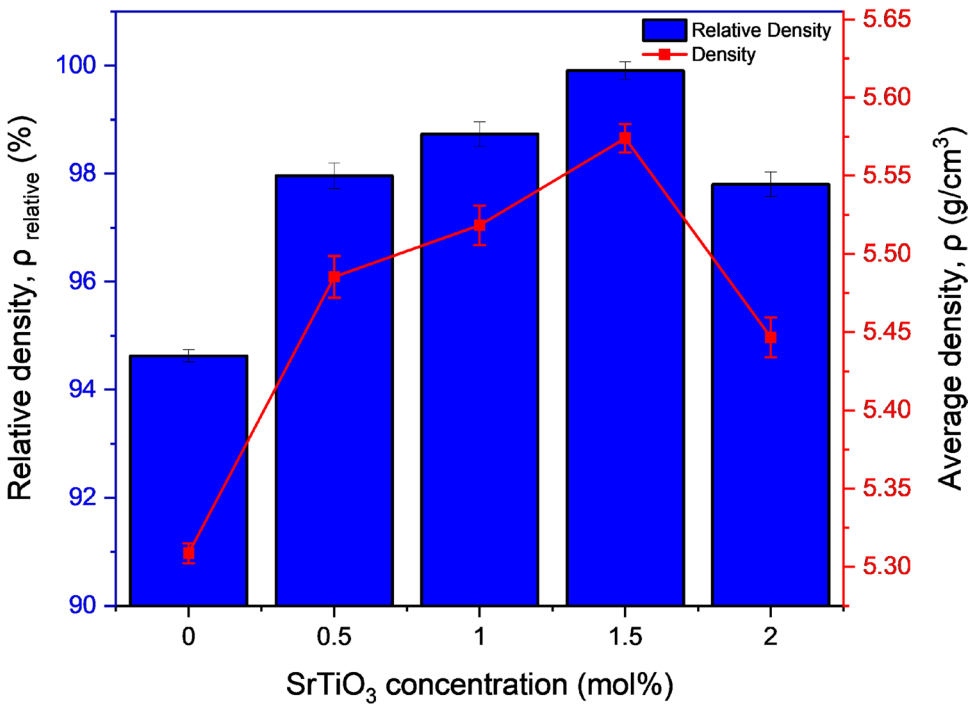

Fig. 4 Graph of relative density and density

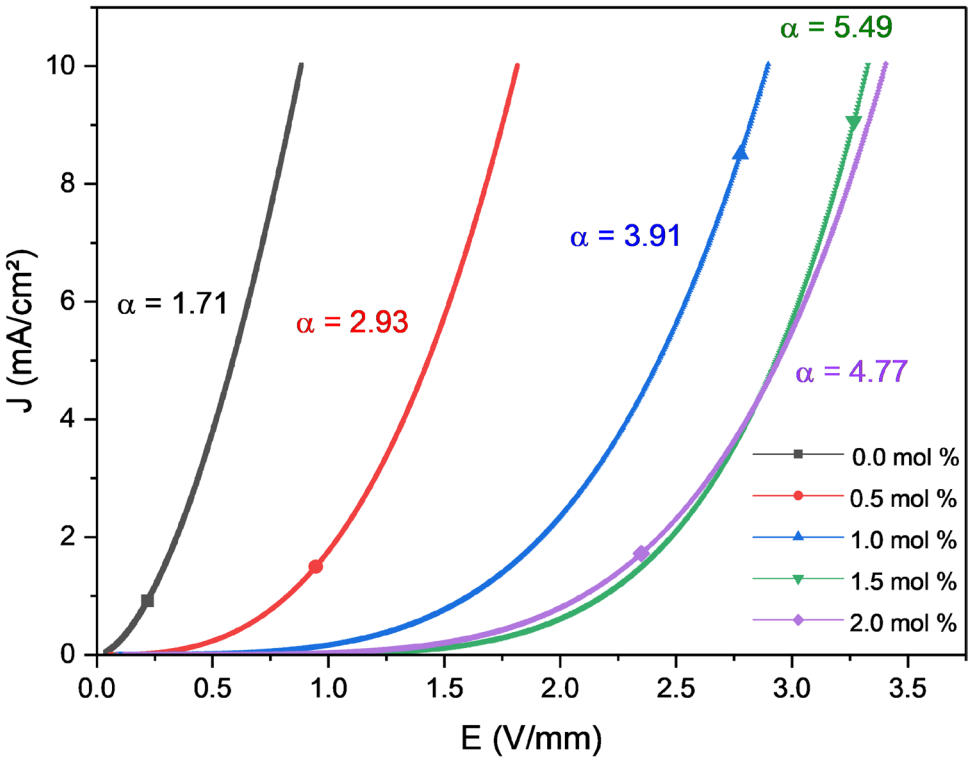

Fig. 5 *J-E* curves of the ZnO doped with different mol concentrations of $SrTiO_3$

and silicate-doped ZnO systems to evaluate its competitiveness. In this work, the ZnO-$SrTiO_3$ ceramic exhibited a breakdown field, E_b, of 2.16 V/mm and a nonlinear coefficient, α, of 5.49. Compared with Fe/Mg/Cu-doped ZnO nanoparticles, which are reported as suitable candidates for a low-voltage varistor with $\alpha = 2.02$ [45], ZnO-$SrTiO_3$ achieves a significantly higher nonlinear coefficient, suggesting better circuit protection for low-voltage applications. Furthermore, in comparison to $CaSiO_3$-doped ZnO ceramics, which demonstrate E_{1mA} values ranging from 0.18 to 0.8 V/mm and α of 2.10 to 4.41 [17], the $SrTiO_3$ dopant proves a higher breakdown voltage, implying that the ZnO-$SrTiO_3$ ceramic varistor can withstand higher electric fields before transitioning to a conductive state. The ability of $SrTiO_3$ to maintain a α at such a low E_b is attributed to the formation of the Zn_2TiO_4 spinel phase and Sr segregation at triple points, which pins grain boundaries more effectively than simple metal doping. This suggests that the ZnO-$SrTiO_3$ composite is a good candidate for surge protection in high-density, low-power microelectronic circuits where conventional high-voltage varistors are unsuitable.

Table 4 Varistor properties of ZnO-$SrTiO_3$ varistors

$SrTiO_3$ (mol%)	α	φ_B (eV)	E_b (V/mm)	J_L (μA/cm^2)
0.0	1.72	0.61	0.37	664.41
0.5	2.93	0.63	0.77	530.89
1.0	3.91	0.65	1.41	435.79
1.5	5.49	0.69	2.16	298.92
2.0	4.77	0.66	1.85	350.18

4 Conclusion

Various concentrations of $SrTiO_3$ have been found to significantly impact the ZnO ceramics. The observed trends in the varistor properties, including the nonlinear coefficient, breakdown voltage, and leakage current, are directly linked to the evolution of the microstructure and density. As the $SrTiO_3$ concentration reached 1.5 mol %, the dopant optimized the material's structure. This improved grain-boundary strength and homogeneity, thereby enhancing electrical performance. The ZnO-$SrTiO_3$ varistor showed the highest α of 5.49, with a low leakage current of 298.92 μA/cm^2 and a breakdown voltage of 2.16 V/mm, suggesting its applicability for low-voltage applications. The adverse effects of phase segregation and reduced

density become dominant beyond this point, compromising the varistor's properties. These findings highlight the importance of precise control over dopant concentration and processing conditions to achieve an optimal balance among microstructure, phases, and electrical performance in $SrTiO_3$-doped ZnO varistors. For future work, further investigations into dielectric spectroscopy as a function of frequency are required to quantify grain boundary capacitance. Additionally, DC aging and surge endurance tests are identified as essential future steps to evaluate the long-term reliability and fatigue resistance of these low-voltage varistor compositions for industrial applications.

Acknowledgements

This research was funded by Universiti Malaysia Terengganu through the Research Intensified Grant Scheme, RIGS (Vot No. 55441). The authors appreciate the analytical support provided by the testing center, Universiti Malaysia Terengganu, Malaysia.

Author contributions

N.H.M.D. conceived and designed the experiments (Conceptualization and Methodology), performed the investigation, analyzed the data (Formal analysis and Software), and wrote the original draft. M.S.S. and I.R.I. contributed to the original draft preparation and editing. N.A.M.N. and A.M.A.A.M.S contributed to the review and editing process. M.S.M.G. was responsible for project administration, funding acquisition, supervision, and writing the original draft. N.H.S. and M.H.M.Z. provided supervision and project administration. All authors reviewed and approved the final manuscript.

Funding

Open access funding provided by The Ministry of Higher Education Malaysia and Universiti Malaysia Terengganu. Universiti Malaysia Terengganu,Vot No. 55441

Data availability

The data that support the findings of this study are available from the corresponding author upon reasonable request.

Declarations

Competing interest The authors declare no competing interests.

References

1. L.F. García, F. Azough, G. Parsons, A. Quadling, B. Wang, R. Freer, Optimising the performance of SiC-based varistors through composition and microstructure control. J. Eur. Ceram. Soc. **42**(20), 600–607 (2022). https://doi.org/10.1016/j.jeurceramsoc.2021.10.034
2. Y.M. Shen, M.C. Len, H.I. Hsiang, Effect of pre-calcination of Bi_2O_3 and Sb_2O_3 on the densification and varistor properties of low-temperature sintered ZnO-Bi_2O_3 ceramics. J. Mater. Sci. Mater. Electron. **34**, 1750 (2023). https://doi.org/10.1007/s10854-023-11209-9
3. P. Xie, Z. Wang, K. Wu, Evolution of intrinsic and extrinsic electron traps at grain boundary during sintering ZnO based varistor ceramics. Materials **15**(3), 1098 (2022). https://doi.org/10.3390/ma15031098
4. T. Tian, L. Zheng, S. Bernik, Z. Man, X. Shi, X. Ruan, G. Li, Influence of Cr_2O_3 doping on the electrical characteristics of novel ZnO-Cr_2O_3-based varistor ceramics. Mater.

Res. Bull. **159**, 11211 (2023). https://doi.org/10.1016/j.materresbull.2022.112111

5. J. Li, K. Tang, S. Yang, D. Zhu, Effects of Sb_2O_3 on the microstructure and electrical properties of ZnO–Bi_2O_3-based varistor ceramics fabricated by two-step solid-state reaction route. Ceram. Int. **47**(14), 19394–19401 (2021). https://doi.org/10.1016/j.ceramint.2021.03.276
6. Y.M. Shen, M.C. Len, H.I. Hsiang, Impact of calcination on low-temperature sintered Bi_2O_3 varistors: Varistor properties and surge current absorption. J. Alloys Compd. **985**, 174084 (2024). https://doi.org/10.1016/j.jallcom.2024.174084
7. M.R. Mendes, I.J. Fernades, C.A.M. Moraes, L.A.L. Santos, W.L. Almeida, V.C. Sousa, Microstructural and electrical properties of the ZnO-Bi_2O_3-MnO_2 system doped with silica obtained from rice husk ash. Ceram. Int. **51**(7), 9398–9411 (2025). https://doi.org/10.1016/j.ceramint.2024.12.373
8. F. Cui, Z. Xu, R. Chu, G. Li, Improving electrical properties of ZnO– Bi_2O_3–Sb_2O_3–MnO_2 varistors by doping with pre-synthesized Bi–Si–O phase. J. Alloys Compd. **836**, 154692 (2020). https://doi.org/10.1016/j.jallcom.2020.154692
9. F. Kharchouche, A. Zebar, Influence of $SrCO_3$-doping on the microstructure and electrical properties of ZnO–(Bi_2O_3/Sb_2O_3) varistor ceramics. J. Mater. Sci. Mater. Electron. **34**(9), 776 (2023). https://doi.org/10.1007/s10854-023-10092-8
10. R. Rohini, C. Pugazhendhi Sugumaran, Enhancement of electro-thermal characteristics of micro/nano ZnO based surge arrester. J. Electr. Eng. Technol. **16**(1), 468–481 (2021). https://doi.org/10.1007/s42835-020-00581-9
11. M. Shi, J. Liu, C. Bing, J. Ming, C. Zhan, J. Yongtao, T. Bin, X. Dong, Effects of In_2O_3 doping on microstructure and electrical properties of ZnO low-voltage varistor. J. Mater. Sci. Mater. Electron. **33**(24), 19242–19251 (2022). https://doi.org/10.1007/s10854-022-08762-0
12. M. Mirzayi, The effect of TiO_2 concentration on the electrical and microstructural properties of ZnO-base varistor ceramic prepared from nanosize ZnO particles. Adv. Appl. Ceram. **119**(7), 373–379 (2020). https://doi.org/10.1080/17436753.2020.1762047
13. H. Feng, Z. Peng, X. Fu, Z. Fu, C. Wang, L. Qi, H. Miao, Effect of TiO_2 doping on microstructural and electrical properties of ZnO-$Pr6O_{11}$-based varistor ceramics. J. Alloys Compd. **497**(1–2), 304–307 (2010). https://doi.org/10.1016/j.jallcom.2010.03.047
14. S.M. Syaizwadi, M.S.M. Ghazali, W.M.K.W.M. Ikhmal, M.A.M.S. Hazim, W.A.W. Rafizah, S. Kassim, O.J. Lee, I.N.R. Aini, S.N. Kamilah, M.H.M. Zaid, M.F.F. Maria, K.A. Matori, Nonlinearity characteristics of low-voltage barium titanate based zinc oxide varistor ceramics modified by cobalt dopants. J. Integr. Circuit Syst. **16**(1), 1–7 (2021). https://doi.org/10.29292/jics.v16i1.220
15. I.I. Lakin, A. Zakaria, Y. Abdollah, D. Umaru, Effect of sintering temperature on microstructure and electrical properties of ZnO + $CaMnO_3$ ceramics used in low-voltage varistors. Dig. J. Nanomater. Biostruct. **10**(1), 189–197 (2015)
16. M. Xu, C. Cai, Y. Shi, M. Xie, Y. Wu, Y. Liu, J. Peng, J. Bao, S. An, The grain growth control of ZnO-V_2O_5 based varistors by $PrMnO_3$ addition. Micromachines **13**(2), 214 (2022)
17. M.A. Badruddin, M.S. Shaifudin, A.M.I.A.A. Mohd, W.M.I.W.M. Kamaruzzaman, N.A.M. Nasir, N. Yusof, C.S. Kien, M.S.M. Ghazali, Electrical and microstructural evaluation of ZnO varistor ceramics with different $CaSiO_3$ contents. Mater. Chem. Phys. **289**, 126464 (2022). https://doi.org/10.1016/j.matchemphys.2022.126464
18. A.E. Mariño-Gámez, M.I. Miranda-López, M.B. Hernández, A.N. Bondarchuk, L. Falcon-Franco, L. García-Ortiz, J.A. Aguilar-Martínez, Varistor performance of a SnO_2-based system doped with low content of $SrTiO_3$. J. Alloys Compd. **880**, 160529 (2021). https://doi.org/10.1016/j.jallcom.2021.160529
19. P. Mao, J. Wang, L. He, L. Zhang, A. Annadi, F. Kang, Q. Sun, Z. Wang, H. Gong, Excellent capacitor-varistor properties in lead-free $CaCu_3Ti_4O_{12}$-$SrTiO_3$ system with a wrinkle structure via interface engineering. ACS Appl. Mater. Interfaces **12**(43), 48781–48793 (2020). https://doi.org/10.1021/acsami.0c13067
20. S. Roy, D. Das, T.K. Roy, Two stage sintering behaviour of Er_2O_3 doped high performance ZnO varistors. J. Eur. Ceram. Soc. **41**, 10 (2021). https://doi.org/10.1016/j.jeurceramsoc.2021.04.009
21. Q.M. Al-Bataineh, M. Telfah, A.A. Ahmad, A.M. Alsaad, I.A. Qattan, H. Baaziz, Z. Charifi, A. Telfah, Synthesis, crystallography, microstructure, crystal defects, optical and optoelectronic properties of ZnO:CeO_2 mixed oxide thin films. Photonics (Basel) **7**(4), 112 (2020). https://doi.org/10.3390/photonics7040112
22. A. Latif, L. Arab, A. Amri, H. Arab, N. Sengouga, T. Tibermacine, Effect of Ga doping on the structural, optical, and electrical properties of ZnO nanopowders elaborated by sol-gel method. Mater. Res. Bull. **178**, 112886 (2024). https://doi.org/10.1016/J.MATERRESBULL.2024.112886
23. L. Wang et al., Effect of the sintering temperature on the electrical properties of Y–Al-doped ZnO varistors. Int. J. Ceram. Eng. Sci. (2025). https://doi.org/10.1002/ces2.10243

24. J. Tian, Y. Wu, H. Tian, Y. Xu, P. Lu, J. Zhao, B. Zhang, The effect of sintering temperature on the microstructure and electrical properties of ZnO–Bi2O3 varistor ceramics. J. Electron. Mater. **53**(27), 3994–4000 (2024). https://doi.org/10.1007/s11664-024-11135-4
25. K. Wang, Y. Zhao, X. Chen, R. Chu, G. Li, Z. Xu, Effects of sintering temperature on microstructure and varistor performances of ZnO-$SrCO_3$-Co_2O_3 ceramics. Ceram. Int. **50**(23), 51162–51171 (2024). https://doi.org/10.1016/j.ceramint.2024.10.031
26. Y. Zhao, Y. Guo, J. Li, P. Li, Efficient hydrogen evolution with ZnO/$SrTiO_3$ S-scheme heterojunction photocatalyst sensitized by Eosin Y. Int. J. Hydrogen Energy **46**(36), 18922–18935 (2021). https://doi.org/10.1016/j.ijhydene.2021.03.051
27. T. Das, B.K. Das, Impact of strontium doping on the structural and NTCR properties of ZnO ceramics. J. Mater. Sci. Mater. Electron. **35**(35), 1–12 (2024). https://doi.org/10.1007/s10854-024-13969-4
28. H. Chen, L. Zheng, J. Zeng, G. Li, Effect of Sr doping on nonlinear current–voltage properties of ZnO-based ceramics. J. Electron. Mater. **50**(7), 4096–4103 (2021). https://doi.org/10.1007/s11664-021-08960-2
29. W. Cao, H. Xu, J. Liu, W. Li, C. Gou, B. Ren, X. Zheng, X. Liang, X. Wang, X. Zhang, Preparation and electrical properties of Er_2O_3-doped ZnO-Cr_2O_3-$SrCO_3$-based varistors with low leakage current density and high aging resistance. Ceram. Int. **51**(26), 49602–49611 (2025). https://doi.org/10.1016/j.ceramint.2025.08.199
30. C.E. Krill, E.A. Holm, J.M. Dake, R. Cohn, K. Holíková, F. Andorfer, Extreme abnormal grain growth: connecting mechanisms to microstructural outcomes. Annu. Rev. Mater. Res. **53**, 319–345 (2023). https://doi.org/10.1146/annurev-matsci-080921-091647
31. N. Yongvanich, Synthesis of strontium-doped ZnO-based nanopowders by chemical co-precipitation. Chiang Mai J. Sci. **40**(6), 1046–1054 (2013)
32. C.M. Montemayor Palos, M.I. Pech-Canul, M.B. Hernández, R.F. Cienfuegos-Pelaes, J.A. Aguilar-Martínez, Impact of the particle size on the non-Ohmic properties of doped ZnO ceramic varistor materials synthesized via mechanosynthesis. Ceram. Int. **51**(3), 3559–3567 (2024). https://doi.org/10.1016/j.ceramint.2024.11.332
33. J. Li, K. Tang, D. Zhu, Effect of Ho_2O_3 doping on the microstructure and electrical properties of ZnO–Bi_2O_3–Sb_2O_3–Cr_2O_3–Co_2O_3–MnO_2-based varistors. Mater. Sci. Semicond. Process. (2023). https://doi.org/10.1016/j.mssp.2022.107180
34. M.S. Shaifudin, M.S.M. Ghazali, W.M.K.W.M. Ikhmal, W. Rafizah, S. Kassim, I.N.Q. Aini, S.N. Kamilah, M.H.M. Zaid, M.F.F. Maria, K.A. Matori, Synergistic effects of Pr_6O_{11} and Co_3O_4 on electrical and microstructure features of ZnO-$BaTiO_3$ varistor ceramics. Materials **14**(4), 702 (2021). https://doi.org/10.3390/ma14040702
35. M.R. Mazlan, N.H. Jamadon, A. Rajabi, A.B. Sulong, I.F. Mohamed, F. Yusof, N.A. Jamal, Necking mechanism under various sintering process parameters – a review. J. Mater. Res. Technol. **23**, 2189–2201 (2023). https://doi.org/10.1016/j.jmrt.2023.01.013
36. N.J. Lóh, L. Simão, C.A. Faller, A. De Noni, O.R.K. Montedo, A review of two-step sintering for ceramics. Ceram. Int. **42**(11), 12556–12572 (2016). https://doi.org/10.1016/j.ceramint.2016.05.065
37. S. Gong, H. Zhao, The effect of B_2O_3 doping on the properties of electrical and thermal conductivity for SnO_2 varistors. Materials (2025). https://doi.org/10.3390/ma18071399
38. K. Wang, Y. Zhang, J. Wu, R. Chu, Z. Xu, Nonlinear property studies of SiO_2-modified ZnO-$SrCO_3$-CoO (ZSC) based varistors thorough Rietveld refinement, structural and electrical characterizations. J. Alloys Compd. **1031**, 180892 (2025). https://doi.org/10.1016/j.jallcom.2025.180892
39. J. Liu, B. Ren, W. Cao, Preparation and electrical properties of Eu_2O_3 doped high-performance ZnO-Bi_2O_3 based varistors. Ceram. Int. **51**(9), 11586–11592 (2025). https://doi.org/10.1016/j.ceramint.2025.01.013
40. B.H. Chen, B.W. Wang, P.Z. Gao, P. Zhang, H.H. Chen, Effects of raw particle size and annealing on microstructure, electrical and mechanical behaviors of ZnO-based varistors. J. Alloys Compd. **872**, 159638 (2021). https://doi.org/10.1016/j.jallcom.2021.159638
41. J. Niu, H. She, Z. Liu, M. Cheng, J. Xu, J. Liu, G. Chen, B. Tang, D. Xu, A current-controlled flash sintering processing leading to dense and fine-grained typical multi-element ZnO varistor ceramics. J. Alloys Compd. **876**, 160124 (2021). https://doi.org/10.1016/j.jallcom.2021.160124
42. I. Markevich, I. Vorona, V. Nosenko, O. Kolomys, V. Strelchuk, T. Stara, L. Borkovska, V. Bondarenko, O. Melnichuk, L. Melnichuk, N. Korsunska, Mn distribution in ZnO:Mn ceramics: influence of sintering process and thermal annealing. ECS J. Solid Stw Sci. Technol. **9**(10), 103001 (2020). https://doi.org/10.1149/2162-8777/abba06
43. P. Meng, X. Zhao, X. Yang, J. Wu, Q. Xie, J. He, J. Hu, J. He, Breakdown phenomenon of ZnO varistors caused by non-uniform distribution of internal pores. J. Eur. Ceram. Soc. **39**(15), 4824–4830 (2019). https://doi.org/10.1016/j.jeurceramsoc.2019.06.043
44. R.K. Sendi, Sensitivity of electrical behaviours of ZnO nanoparticle–Bi_2O_3–Mn_2O_3 varistor system to various

La_2O_3 doping compositions. J. Taibah Univ. Sci. **16**(1), 903–911 (2022). https://doi.org/10.1080/16583655.2022.2119740

45. G. Taka, T.D. Das, Synthesis and application of Fe/Mg/Cu-doped ZnO nanoparticles in humidity sensors and low-voltage varistors. Phys. B Condens. Matter (2025). https://doi.org/10.1016/j.physb.2025.417228